Highly polarized light from stable ordered magnetic fields in GRB 120308A

C. G. Mundell[1], D. Kopač[2], D. M. Arnold[1], I. A. Steele[1], A. Gomboc[2,3], S. Kobayashi[1], R. M. Harrison[1], R. J. Smith[1], C. Guidorzi[4], F. J. Virgili[1], A. Melandri[5] & J. Japelj[2]

After the initial burst of γ-rays that defines a γ-ray burst (GRB), expanding ejecta collide with the circumburst medium and begin to decelerate at the onset of the afterglow, during which a forward shock travels outwards and a reverse shock propagates backwards into the oncoming collimated flow, or 'jet'[1,2]. Light from the reverse shock should be highly polarized if the jet's magnetic field is globally ordered and advected from the central engine[3,4], with a position angle that is predicted to remain stable in magnetized baryonic jet models[5] or vary randomly with time if the field is produced locally by plasma or magnetohydrodynamic instabilities[6,7]. Degrees of linear polarization of $P \approx 10$ per cent in the optical band have previously been detected in the early afterglow[6,8], but the lack of temporal measurements prevented definitive tests of competing jet models[9–14]. Hours to days after the γ-ray burst, polarization levels are low ($P < 4$ per cent), when emission from the shocked ambient medium dominates[15–17]. Here we report the detection of $P = 28^{+4}_{-4}$ per cent in the immediate afterglow of Swift γ-ray burst GRB 120308A, four minutes after its discovery in the γ-ray band, decreasing to $P = 16^{+5}_{-4}$ per cent over the subsequent ten minutes. The polarization position angle remains stable, changing by no more than 15 degrees over this time, with a possible trend suggesting gradual rotation and ruling out plasma or magnetohydrodynamic instabilities. Instead, the polarization properties show that GRBs contain magnetized baryonic jets with large-scale uniform fields that can survive long after the initial explosion.

On 8 March 2012 at $T_0 = 06:13:38$ UT, NASA's Swift satellite identified GRB 120308A as a single, broad pulse of γ-rays lasting approximately 100 s, beginning at $T_0 – 30$ s, peaking at $\sim T_0 + 1$ s and ending at $\sim T_0 + 70$ s (ref. 18). The Swift X-ray telescope began observing the GRB at $T_0 + 92.6$ s, identifying a bright X-ray afterglow with a light curve exhibiting the canonical behaviour of a typical long GRB. The Liverpool Telescope responded automatically to the Swift trigger and identified the optical afterglow[19].

Polarimetry was performed using the purpose-built RINGO2 polarimeter[20] on the Liverpool Telescope (see Supplementary Information). RINGO2 observations of GRB 120308A started at 06:17:38 UT ($T_0 + 240$ s) and ended at 06:27:25 UT. During that time, a total of 5,600 images were taken (700 at each angle of the Polaroid polarizer; Fig. 1a). After correcting for instrumental effects, co-adding the data at each rotator angle over that period showed a strong time-averaged polarization signal from the GRB of $P \approx 20\%$ compared with values $P < 3\%$ for the other objects of similar brightness in the image (Fig. 1b).

The time-sampled polarization over this period is both high and variable, with $P = 28 \pm 4\%$ declining to $P = 16^{+5}_{-4}\%$ by ~ 800 s after the GRB trigger (Fig. 2a), in contrast to unpolarized comparison objects in the GRB field of view, which straddle the GRB brightness and location and show no significant variation over the same time. The GRB polarization position angle θ is remarkably stable over this period (Fig. 2b), with a total variation that does not exceed $\theta \approx 15°$ and which shows a

trend that may be consistent with gradual rotation of the angle, ruling out plasma or magnetohydrodynamic instabilities[6,7]. The measured polarization evolution is also robust to different choices of temporal binning. The derived extinction local to the GRB would induce less than 1% of polarization in the GRB afterglow; the high detected polarization in GRB 120308A and the observed temporal variation are therefore intrinsic to the GRB and not due to dust scattering or instrumental effects (see Supplementary Information).

Following the RINGO2 exposures, a series of Liverpool Telescope RATCam optical images was collected until twilight made data collection no longer possible. The corresponding time evolution of the optical flux density using measurements from both RINGO2 and RATCam is shown as a light curve in Fig. 2c, in which the optical flux density reaches a peak at $\sim T_0 + 300$ s, followed by a steady fade of the emission with a possible plateau around $\sim T_0 + 1,000$ s.

In the standard 'reverse plus forward shock' scenario[2], emission from both shocks contribute to the afterglow; their relative brightnesses and temporal evolution combine to produce the observed light curve. Empirically, optical light curves are commonly fitted with a collection of double broken power laws[21] in an attempt to parametrize the individual contributions from reverse and forward shocks to the overall shape of the light curve. The light curve of GRB 120308A can either be parametrized with a single peak (which contains equal contributions from reverse and forward shock emission[22]) or with two peaks (of different brightness and separated in time[8] such that the reverse shock peak dominates the light curve at early time and the later emergence of the forward shock accounts for the flattening of the light curve at $\sim 1,000$ s; see Supplementary Information). In both cases, the peak at $\sim T_0 + 300$ s represents the onset of deceleration of the fireball and the emission at that time contains a significant contribution from the reverse shock.

Using the relative strengths of reverse- and forward-shock emission in both scenarios, we derive an independent estimate of the jet's magnetization[23]; the magnetic energy density in the reverse-shock region is higher than in the forward-shock region by a factor of ~ 30 for the one-peak model and by a factor >500 for the two-peak case. In both cases, a magnetized reverse shock is required, consistent with the high degree of polarization detected.

Figure 3 shows degree of polarization as a function of time after the burst in the cosmological rest frame; GRB 120308A is shown in the context of previous polarization measurements of other GRBs at early and late times. At $P = 28\%$, the optical polarization measured in GRB 120308A is significantly higher than previous detections. Tangled magnetic fields produced locally in a shock front produce low net polarization of a few per cent (ref. 15), as seen at late time, and random temporal change in polarization angle. They are therefore excluded as the origin of polarized optical emission in GRB 120308A. Instead, a magnetized reverse shock with an ordered magnetic field is needed to explain the large net polarization and stable position angle in GRB 120308A.

[1]Astrophysics Research Institute, Liverpool John Moores University, IC2, Liverpool Science Park, 146 Brownlow Hill, Liverpool L3 5RF, UK. [2]Faculty of Mathematics and Physics, University of Ljubljana, Jadranska ulica 19, 1000 Ljubljana, Slovenia. [3]Centre of Excellence SPACE-SI, Aškerčeva cesta 12, 1000 Ljubljana, Slovenia. [4]Physics Department, University of Ferrara, Via Saragat, 1, 44122 Ferrara, Italy. [5]INAF/Brera Astronomical Observatory, via Bianchi 46, 23807, Merate (LC), Italy.
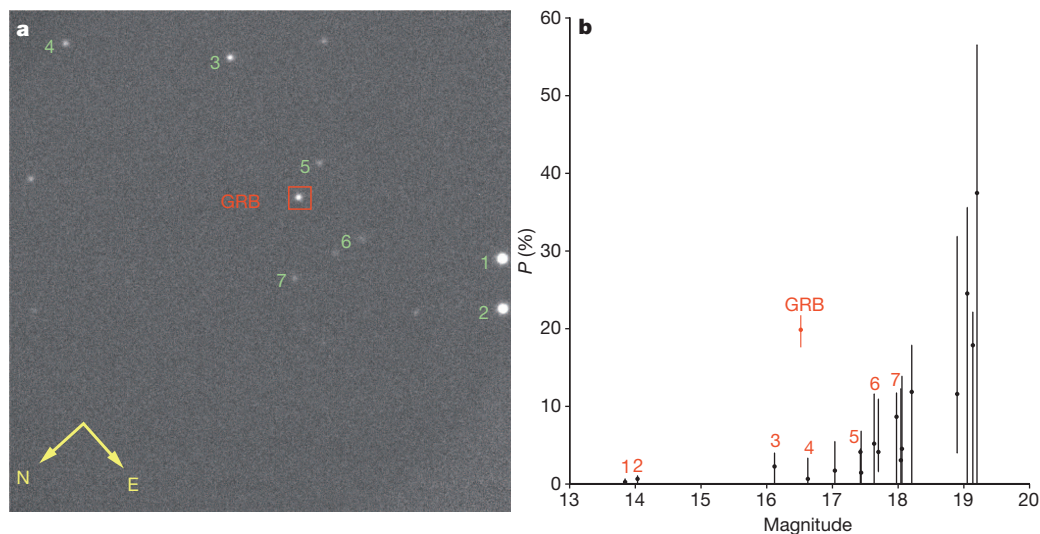
Figure 1 | Time-integrated optical properties of the GRB 120308A field.
a, RINGO2 total intensity image of $4' \times 4'$ field containing GRB 120308A, with total exposure time 588 s. The GRB (boxed) and seven comparison objects (numbered) are indicated; the directions of north and east are shown. RINGO2 combines a Polaroid polarizer rotating at ~1 revolution s^{-1} with a fast readout electron multiplying CCD camera that is triggered eight times per revolution. Summing data from each rotation angle allows derivation of the total intensity for each source in the image, while analysis of their relative intensities allows calculation of their Stokes parameters[25]. Measurements are not affected by variations in source brightness or observing conditions on timescales >1 s owing to the rapid rotation of the polaroid. There is no significant variation in atmospheric transparency or seeing (image point-spread function) over the 588-s exposure. **b**, Measured time-averaged polarization P of all objects versus apparent magnitude. As P is a one-sided (always positive) quantity, noise in the Stokes q and u parameters translates into a rising P with large uncertainty for the faintest objects, even though their actual polarization is likely to be small. The strong time-averaged polarization of the GRB (red symbol) of 20% compared to sources of similar brightness is obvious. Error bars ($\pm 1\sigma$) were calculated using a Monte Carlo simulation ($N = 10,000$). This used a range of input q and u values with an error distribution calculated from the combination of photon counting statistics with the uncertainty in instrumental calibration to calculate 1σ ranges of P and position angle (θ) for each object. All quoted measurements in this Letter use this Monte Carlo estimator, although because polarization in GRB 120308A is significantly non-zero, the derived errors (within ~1% absolute error) are comparable to standard error analyses for that object (see Supplementary Information and Extended Data Figs 1, 2, 3, 4, 5, 6).

The theoretical maximum degree of linear polarization of synchrotron radiation emitted by electrons in a perfectly homogeneous magnetic field is $P \approx 70\%$; the difference between the measured and the theoretical maximum can therefore provide further constraints on the physical properties of the emitting source. The measured net polarization can be less than the theoretical maximum because of (1) the dilution of polarized reverse-shock emission by unpolarized forward-shock emission, (2) the combination of ordered magnetic fields from the central
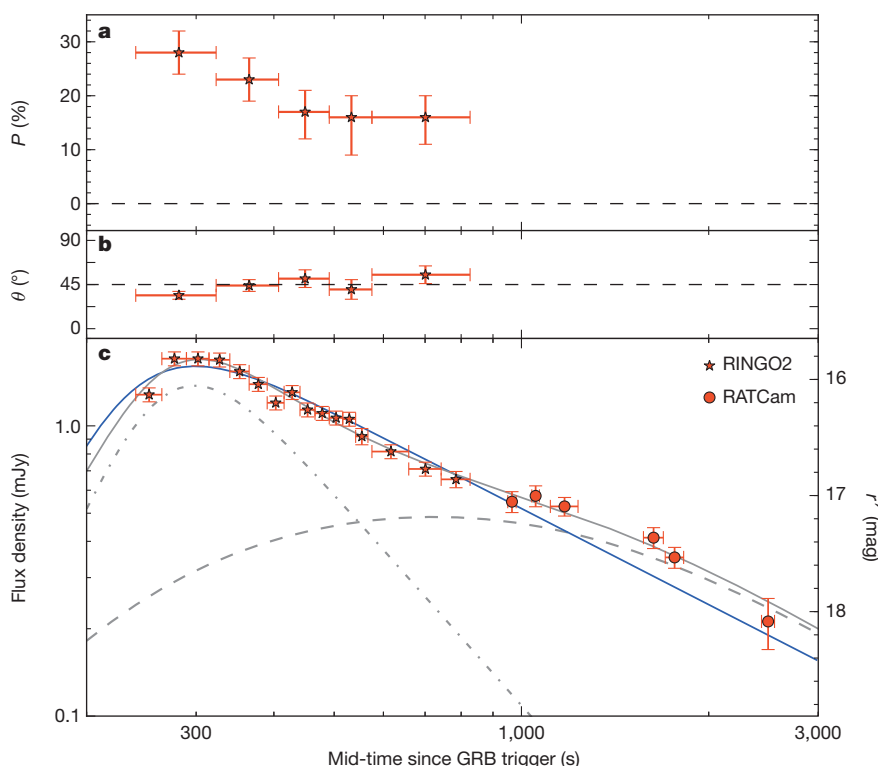

Figure 2 | Evolution of optical polarization and brightness in GRB 120308A. a, **b**, Evolution of polarization degree P (**a**) and position angle θ (**b**; degrees east of north) for GRB 120308A. Individual 0.125-s RINGO2 exposures at the eight Polaroid angles are co-added over a desired time interval into eight images, on which absolute aperture photometry is performed and P and θ derived. Owing to the low read noise of the system, data from each rotation angle can be stacked into temporal bins after data acquisition to optimize signal-to-noise ratio versus time resolution. Here the data were subdivided into four bins of duration ~84 s and one bin of ~252 s giving roughly equal signal-to-noise ratio. The observed polarization properties are robust to alternative choices of temporal binning (see Supplementary Information and Extended Data Figs 7, 8, 9). Error bars, $\pm 1\sigma$, as described in Fig. 1b. **c**, Light curve of GRB 120308A in red (555–690 nm) light using RINGO2 and RATCam. Data have been cross-calibrated to the SDSS r' system via five objects in common, with a possible systematic error of up to ~6% between the two instruments due to colour effects. Model fits using one peak (blue solid line) or two peaks (broken grey line for each component; resultant combined light curve in solid grey) are shown with an additional point[26] constraining late time behaviour (see Supplementary Information). The two-peak model is statistically slightly preferred. Error bars, $\pm 1\sigma$.
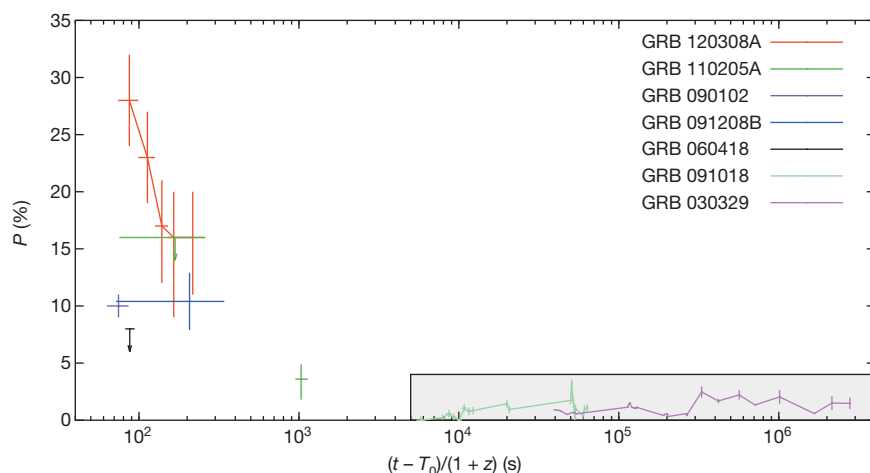
Figure 3 | Rest-frame optical polarization properties of GRBs. The degree of optical polarization P is plotted as a function of time after the burst in the cosmological rest frame, $(t - T_0)/(1 + z)$, where z is redshift and $(t - T_0)$ is the time after the burst in the observer frame. GRB 120308A, GRB 110205A[27], GRB 091208B[6], GRB 090102[8] and GRB 060418[22] were measured at early time. The shaded area shows the typical polarization levels of GRBs measured at late times; representative examples GRB 091018[17] and GRB 030329[16] are shown. Polarization error bars are as reported in the corresponding publications; the temporal error bars show the duration of the measurement. See Supplementary Information and Extended Data Fig. 10 for the determination of redshift for GRB 120308A.

engine and tangled local magnetic fields, (3) a toroidal magnetic field viewed slightly off-axis to the jet axis or (4) large-scale magnetic fields (including toroidal field) that are distorted on an angular scale $1/\Gamma$ corresponding to the relativistically beamed observable scale around the line of sight (here Γ is the Lorentz factor). All four scenarios could apply to the single-peak model. In the two-peak model, scenarios (1) and (2) are excluded owing to the dominant reverse-shock emission and high magnetization. Regardless of the particular model, the polarization characteristics reported here probe an important phase—previously unseen—in the evolution of the physical conditions in the relativistic jet. The large-scale field required in GRB 120308A may not be perfectly homogeneous, even in the small observable angular scale $\sim 1/\Gamma$, and small distortions in the field lines could cause a slight change in the polarization position angle; the trend observed in GRB 120308A will provide new constraints on jet models.

We note that although the radiation mechanism responsible for prompt γ-ray emission has not yet been firmly established, the large values of γ-ray polarization in GRB 110301A and GRB 110721A[24], if confirmed in other GRBs, provide complementary evidence for magnetic fields in the ejecta. The high degree of optical polarization detected in GRB 120308A and its stable position angle shows that large-scale fields survive long after the burst. In the future, detection of optical, γ-ray and microwave polarization properties in the same GRB would provide valuable insight into the full evolution of the magnetic field.

Online Content Any additional Methods, Extended Data display items and Source Data are available in the online version of the paper; references unique to these sections appear only in the online paper.

1. Piran, T. Gamma ray bursts and the fireball model. *Phys. Rep.* **314,** 575–667 (1999).
2. Zhang, B., Kobayashi, S. & Mészáros, P. Gamma-ray burst early optical afterglows: implications for the initial Lorentz factor and the central engine. *Astrophys. J.* **595,** 950–954 (2003).
3. Granot, J. & Königl, A. Simulations of ultrarelativistic magnetodynamic jets from gamma-ray burst engines. *Astrophys. J.* **594,** L83–L87 (2003).
4. Lyutikov, M. Explosive reconnection in magnetars. *Mon. Not. R. Astron. Soc.* **346,** 540–554 (2003).
5. Lazzati, D. et al. On the jet structure and magnetic field configuration of GRB 020813. *Astron. Astrophys.* **422,** 121–128 (2004).
6. Uehara, T. et al. GRB 091208B: first detection of the optical polarization in early forward shock emission of a gamma-ray burst afterglow. *Astrophys. J.* **752,** L6 (2012).
7. Gruzinov, A. & Waxman, E. Gamma-ray burst afterglow: polarization and analytic light curves. *Astrophys. J.* **511,** 852–861 (1999).
8. Steele, I. A., Mundell, C. G., Smith, R. J., Kobayashi, S. & Guidorzi, C. Ten percent polarized optical emission from GRB 090102. *Nature* **462,** 767–769 (2009).
9. Medvedev, M. V. & Loeb, A. Generation of magnetic fields in the relativistic shock of gamma-ray burst sources. *Astrophys. J.* **526,** 697–706 (1999).
10. Lyutikov, M. The electromagnetic model of gamma-ray bursts. *New J. Phys.* **8,** 119–123 (2006).
11. Granot, J. The effects of sub-shells in highly magnetized relativistic flows. *Mon. Not. R. Astron. Soc.* **421,** 2467–2477 (2012).
12. Komissarov, S. S. Shock dissipation in magnetically dominated impulsive flows. *Mon. Not. R. Astron. Soc.* **422,** 326–346 (2012).
13. Zhang, B. & Yan, H. The internal-collision-induced magnetic reconnection and turbulence (ICMART) model of gamma-ray bursts. *Astrophys. J.* **726,** 90 (2011).
14. Tchekhovskoy, A., McKinney, J. C. & Narayan, R. Simulations of ultrarelativistic magnetodynamic jets from gamma-ray burst engines. *Mon. Not. R. Astron. Soc.* **388,** 551–572 (2008).
15. Covino, S. GRB 990510: linearly polarized radiation from a fireball. *Astron. Astrophys.* **348,** L1–L4 (1999).
16. Greiner, J. et al. Evolution of the polarization of the optical afterglow of the γ-ray burst GRB 030329. *Nature* **426,** 157–159 (2003).
17. Wiersema, K. et al. Detailed optical and near-infrared polarimetry, spectroscopy and broad-band photometry of the afterglow of GRB 091018: polarization evolution. *Mon. Not. R. Astron. Soc.* **426,** 2–22 (2012).
18. Baumgartner, W. H. et al. GRB 120308A: Swift detection of a burst. *GCN Circ.* **13017** (2012).
19. Virgili, F. et al. GRB 120308A: Liverpool Telescope optical afterglow candidate. *GCN Circ.* **13018** (2012).
20. Steele, I. A. et al. RINGO2: an EMCCD-based polarimeter for GRB followup. *Proc. SPIE* **7735,** 773549 (2010).
21. Beuermann, K. VLT observations of GRB 990510 and its environment. *Astron. Astrophys.* **352,** L26–L30 (1999).
22. Mundell, C. G. et al. Early optical polarization of a gamma ray burst afterglow. *Science* **315,** 1822–1824 (2007).
23. Harrison, R. M. & Kobayashi, S. Magnetization degree of gamma-ray burst fireballs: numerical study. *Astrophys. J.* **772,** 101 (2013).
24. Yonetoku, D. et al. Magnetic structures in gamma-ray burst jets probed by gamma-ray polarization. *Astrophys. J.* **758,** L1 (2012).
25. Clarke, D. & Neumayer, D. Experiments with a novel CCD stellar polarimeter. *Astron. Astrophys.* **383,** 360–366 (2002).
26. Bikmaev, I. et al. GRB 120308A: RTT150 optical observations. *GCN Circ.* **13030** (2012).
27. Cucchiara, A. et al. Constraining gamma-ray burst emission physics with extensive early-time, multiband follow-up. *Astrophys. J.* **743,** 154 (2011).

Author Contributions C.G.M.: instrument science case, observations, scientific interpretation, paper writing lead. I.A.S.: instrument design and build, data calibration. D.K., D.M.A., R.J.S., A.M.: data reduction, analysis and instrument calibration. A.G.: science case, observations, scientific interpretation. C.G., F.J.V., J.J.: observations, data analysis, energy, redshift derivations and afterglow identification. S.K., R.M.H.: scientific and theoretical interpretation. All authors contributed to the writing/editing of the paper and overall scientific interpretation.
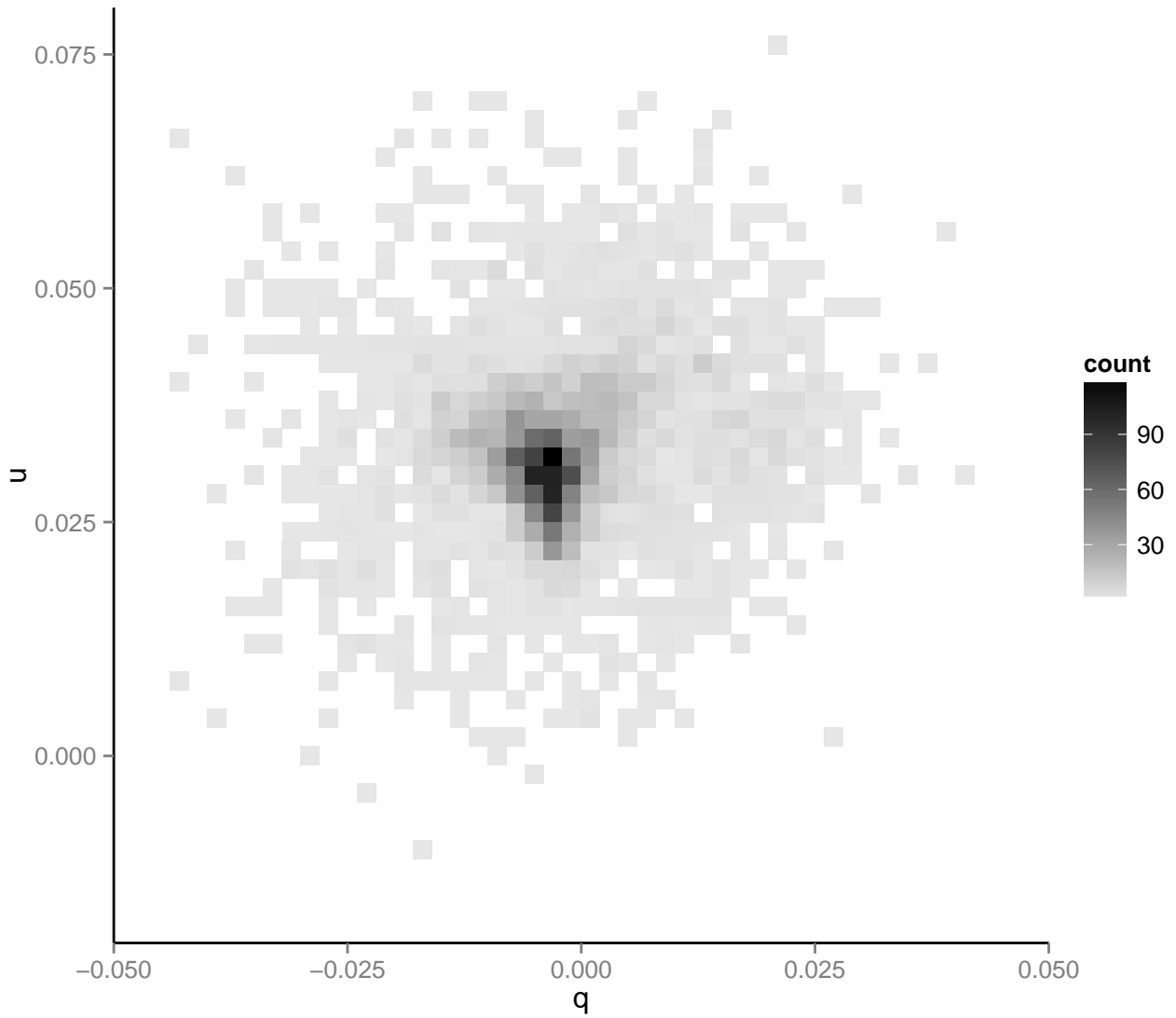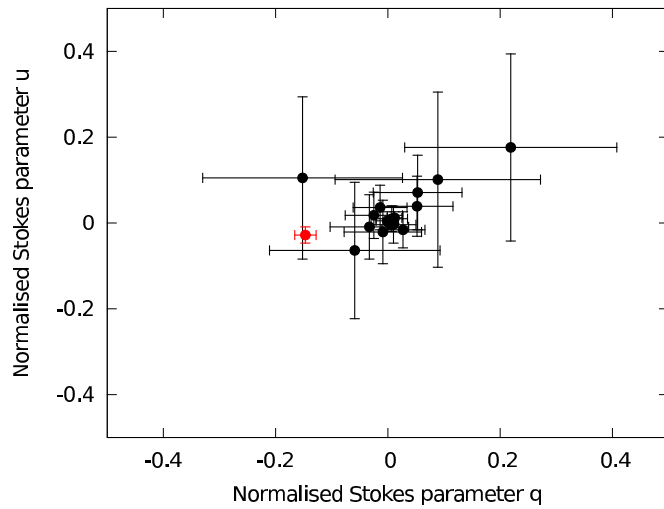
Extended Data Figure 1 | RINGO2 measurements of Stokes parameters for zero-polarized stars. Shown is a two-dimensional histogram depicting the distribution of q values versus u values, with bin size 0.002 in both coordinates, for 3,955 objects with $r' < 16$ mag detected in ~2,000 observations of zero-polarized standard star fields. See Supplementary Information for more details.
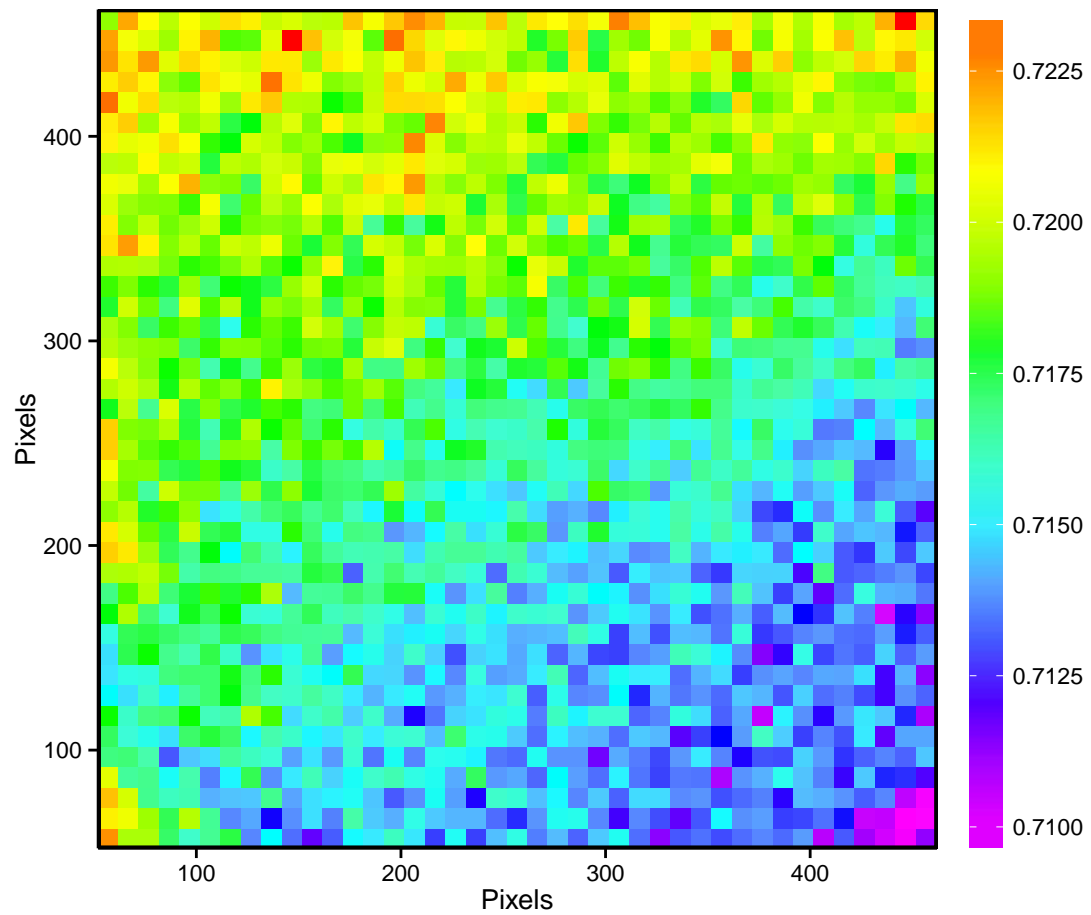
**Extended Data Figure 2 | RINGO2 measurement of the polarization of the zenith sky at sunset over a 4′ × 4′ field of view.** See Supplementary Information for more details.

Extended Data Figure 3 | RINGO2 measurement of Stokes parameters for all objects in the GRB field. The complete data set (all temporal bins) has been used. The GRB optical counterpart is indicated in red. The four points with large error bars are too faint ($r' > 18.5$ mag) for reliable measurements to be made. Error bars are given at 1σ confidence. See Supplementary Information for more details.
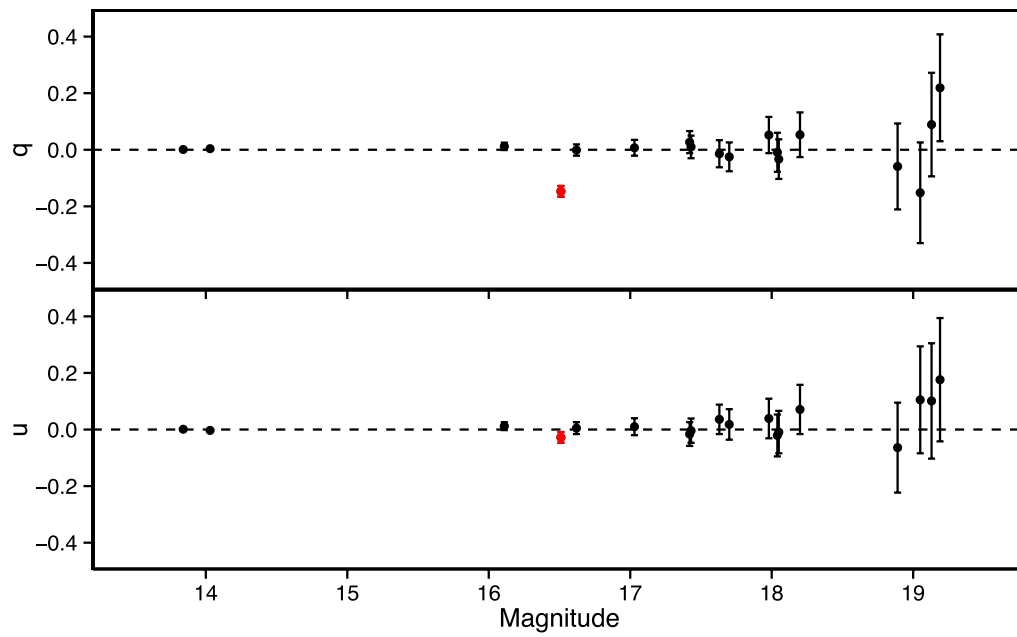
Extended Data Figure 4 | Stokes *q* and *u* parameters of all objects in the GRB field versus *r′* magnitude. Error bars are given at 1σ confidence. See Supplementary Information for more details.
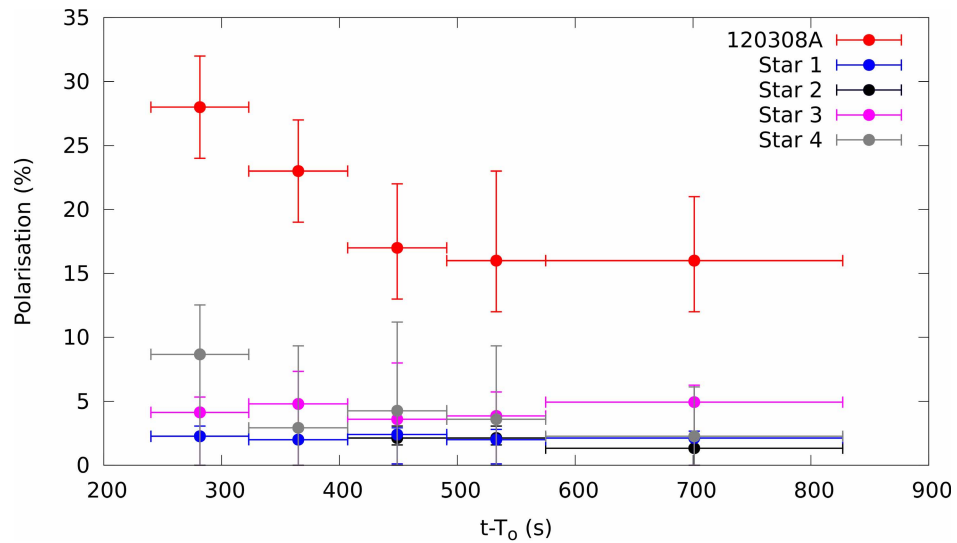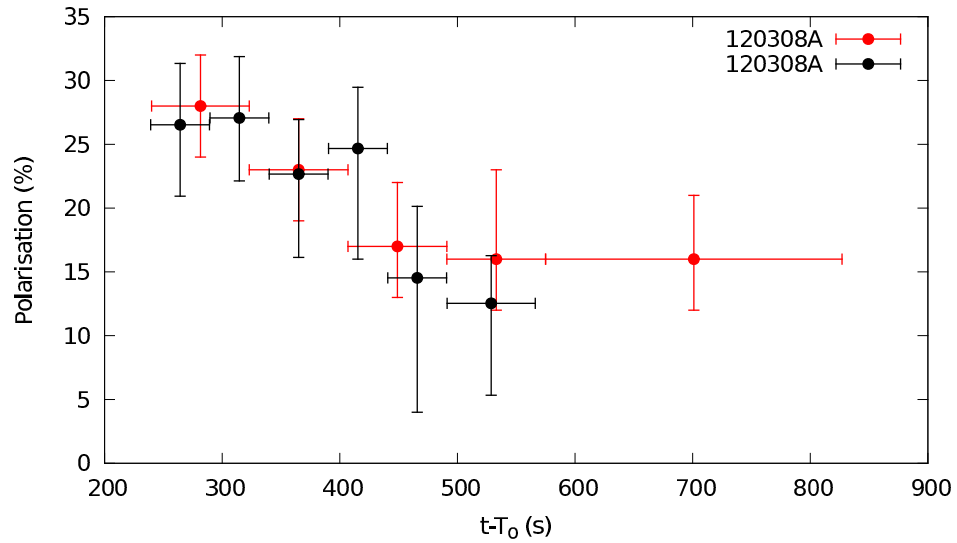
Extended Data Figure 5 | Polarization evolution of GRB 120308A compared with the four brightest objects 1–4 (Fig. 1) in the field. The data have been split into the same five temporal bins as presented in the main text. In comparison with the GRB, no significant variation of the comparison objects is apparent. Error bars are given at 1σ confidence. See Supplementary Information for more details.
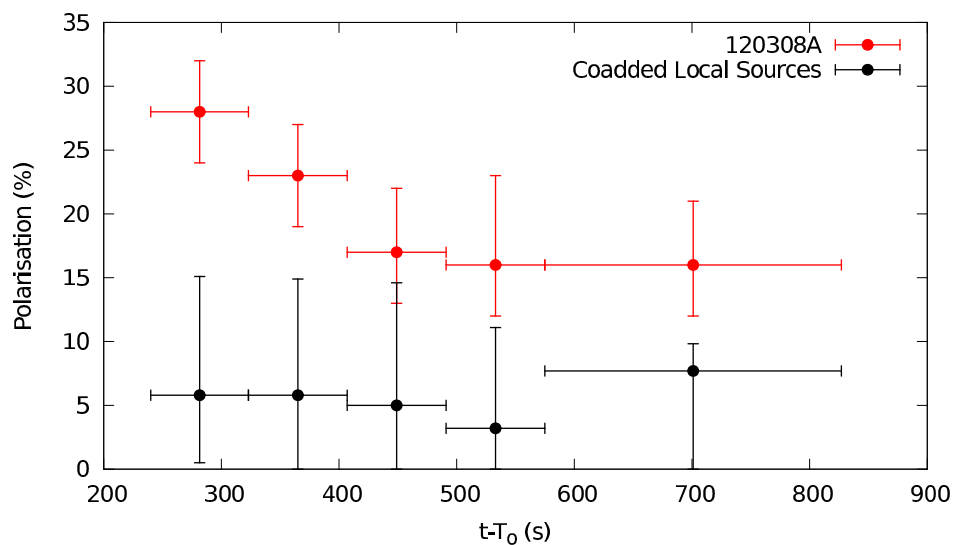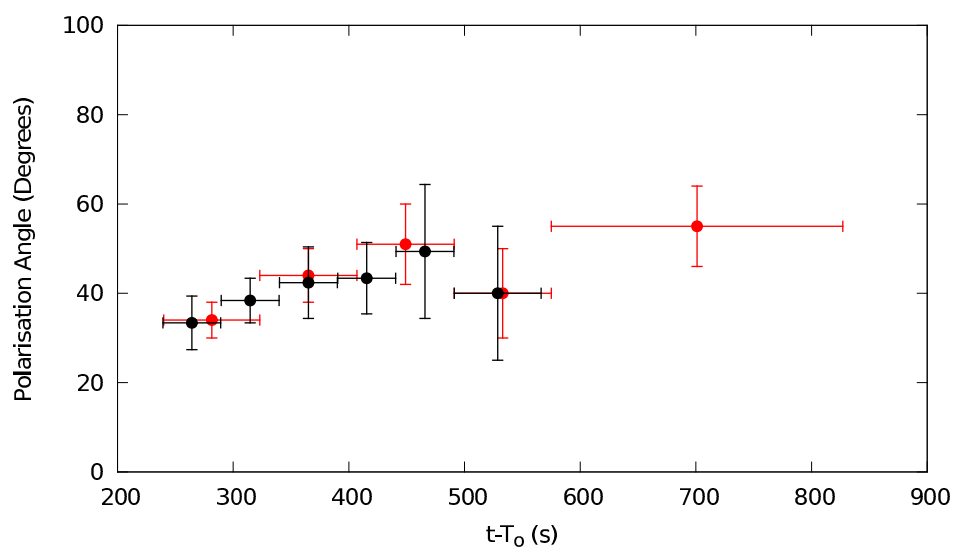
Extended Data Figure 6 | Polarization evolution of GRB 120308A compared with a co-addition of three nearby objects in the field. In order to enhance the signal-to-noise ratio, the data for objects 5–7 (Fig. 1) have been co-added to produce a source of apparent magnitude similar to that of the GRB. The data have been split into the same five temporal bins as presented in the main text. See Supplementary Information for more details.
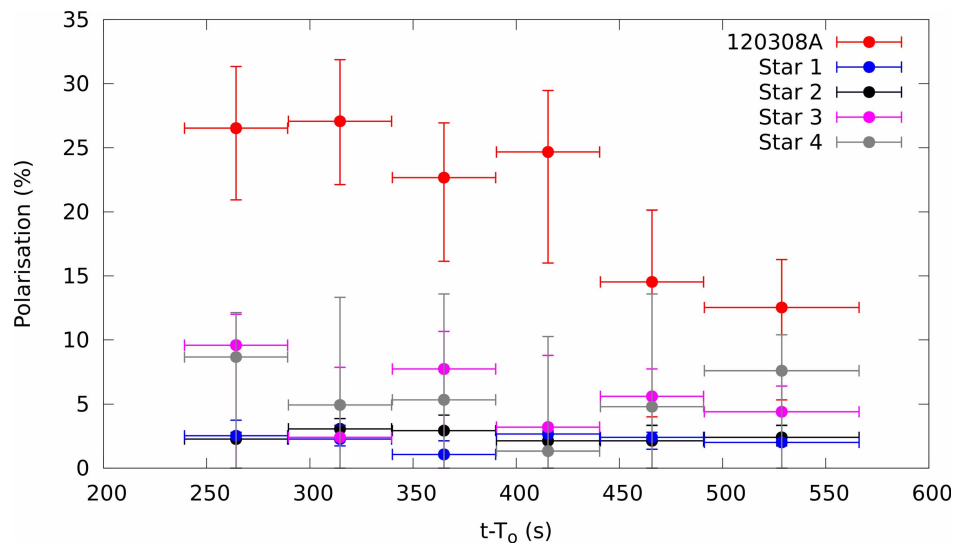
Extended Data Figure 7 | Polarization degree evolution of GRB 120308A with two different temporal binning schemes. Shown is original (red) and an alternative co-addition (black) of the data over the time period covered by the first four temporal bins into six bins. The polarization evolution of the optical counterpart is unaffected within the error bars. Error bars are given at 1σ confidence. See Supplementary Information for more details.

Extended Data Figure 8 | Polarization angle evolution of GRB 120308A with two different temporal binning schemes. Original (red) and an alternative co-addition (black) of the data over the time period covered by the first four temporal bins into six bins. The evolution of the polarization angle is unaffected within the error bars. Error bars are given at 1σ confidence. See Supplementary Information for more details.

Extended Data Figure 9 | Polarization evolution of GRB 120308A compared with the four brightest objects in the field for alternative temporal binning. The data have been split into six temporal bins covering the first 305 s of observation. As in Extended Data Fig. 5, in comparison with the GRB no significant variation of the comparison objects is apparent. Error bars are given at 1σ confidence. See Supplementary Information for more details.
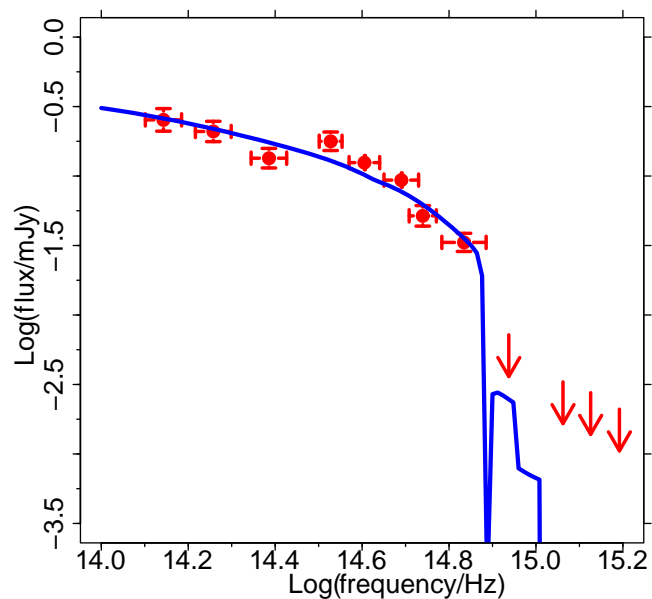
Extended Data Figure 10 | Spectral energy distribution and best fit model for GRB 120308A. Flux density at $t = 1.44\,$h after the GRB is plotted as a function of observing frequency. Upper limits are given at 3σ confidence. Error bars are given at 1σ confidence. See Supplementary Information for more details.